A FEM/DEM adaptive remeshing strategy for brittle elastic failure initiation and propagation

Farouk Yahya, Cédric Hubert, Nicolas Leconte, Laurent Dubar

Received: Added at production | Revised: Added at production | Accepted: Added at production

DOI: xxx/xxxx

RESEARCH ARTICLE

A FEM/DEM adaptive remeshing strategy for brittle elastic failure initiation and propagation

Farouk Yahya[1] | **Cédric Hubert**[1,2] | **Nicolas Leconte**[1,3] | **Laurent Dubar**[1]

[1]UPHF, CNRS, UMR 8201 - LAMIH, Valenciennes, France

[2]INSA Hauts-de-France, Valenciennes, France

[3]ONERA/DMAS, Lille, France

Correspondence
Cédric Hubert, Université Polytechnique Hauts-de-France, Campus Mont Houy, 59313 Valenciennes Cedex 9, France
Email: cedric.hubert@uphf.fr

Present address
Université Polytechnique Hauts-de-France, Campus Mont Houy, 59313 VALENCIENNES Cedex 9, France

Abstract

This paper presents an adaptive remeshing strategy between the Finite Element Method (FEM) and the Discrete Element Method (DEM). To achieve this strategy, an edge-to-edge coupling method based on Lagrange multipliers has been set-up to ensure the continuity of velocities at the interface. To switch from a computation initially purely FEM to a FEM-DEM one, a field transfer method was required. In particular, a displacement field transfer method has been set-up. The switching from a FEM subdomain to a DEM one is activated by a transition criterion. Each time a FEM subdomain is substituted by a DEM one, the DEM subdomain microscopic properties are set-up with respect to the subdomain geometry and desired particle refinement. This is performed thanks to the linking to the so-called "Cooker", a tool distributed along with the GranOO Workbench. Two subdomain remeshing cases were dealt with: that of an initially FEM subdomain that is converted to DEM, and that of DEM subdomains which coalesce. A first numerical test case shows that the dynamic remeshing method behaves as expected: FEM subdomains are substituted by DEM ones when the transition criterion is met, and DEM subdomains coalesce when required. A second numerical test case shows a good agreement with a crack propagation experiments of the litterature.

KEYWORDS
Finite Element Method, Discrete Element Method, Remeshing, Coupling method, Field transfer method

1 | INTRODUCTION

The phenomenology of brittle fracture is frequently observed in structural systems, whether they originate from fields such as aerospace, automotive, or civil engineering. This historical observation has stimulated the development of theoretical and experimental methodologies aimed at anticipating the emergence and propagation of damage within these structures. Among these methodologies, the Kalthoff experiment[1], for instance, allows the observation of dynamic crack propagation in mixed mode. Furthermore, the Compact Compression Specimen (CCS)[2] is another experiment that offers the opportunity to study mixed crack mode with a complex geometry. In the same context, one can also mention the John-Shah[3] experiment and various variants of the Kalthoff experiment, such as those developed by Zhou-Rosakis-Ravichandran[4].
The numerical simulation represents the least costly solution when compared to experimental studies for predicting crack propagation and its influence on structures. However, the use of the Finite Element Method (FEM) reaches its limits due to the discontinuities caused by cracking, which contradicts the continuity assumption on which this method relies, rendering its application impossible.

Advanced methods based on the FEM, more precisely, continuum mechanics, have been developed (Cohesive Zone Model[5], XFEM[6], PhaseField[7]) to account for cracking in materials. Each method possesses its own limitations. The Cohesive Zone Model requires the knowledge of the location of discontinuities in the displacement field during the building of the Finite Element (FE) mesh, leading to a strong dependence between crack paths and the topology of the FE mesh[8]. The XFEM method is not well-suited for modeling dynamic fracture that involves the creation, expansion, and merging of a large number of cracks[9].

Abbreviations: FEM, Finite Element Method; DEM, Discrete Element Method; FE, Finite Element; DE, Discrete Element; CD, Central Difference.

The limitations of PhaseField models become apparent when an initial crack formation needs to be performed in an undamaged material. In such situations, these models tend to predict a significant decrease in stiffness before the crack actually forms [10].

The Discrete Element Method (DEM) finds its main application in modeling discontinuous media such as powders or granular materials [11]. Some specific subcategories of DEM, known as Lattice Element Methods [12,13,14,15], allow the modeling of continuous media by introducing interaction laws between particles. These laws enable simulating the apparent behavior of the material by calibrating local parameters appropriately. The DEM is widely recognized for its ability to accurately model discontinuities. Among these discontinuities, material fractures are included, which are simulated by breaking the links between Discrete Elements (DE). This distinctive feature gives the DEM remarkable reliability in simulating crack propagation in brittle materials [16]. Thanks to this approach, it is possible to analyze in detail and realistically the behavior of these materials when subjected to significant stresses or to optimize their design to enhance their resistance to rupture.
However, it is important to note that the use of the DEM requires significant computational capabilities due to the high computational costs associated with this method.

Some authors have sought to take advantage of the benefits of both FEM and DEM by developing coupling approaches, with overlap such as the Bridging domain method [17,18], the Separate domain coupling method [19] and the Separate edge coupling method [20], or without overlap such as the Edge-to-edge coupling method [21,22,23,24]. These approaches allow modeling a specific region using DE to account for cracking, while other distant regions whose contribution to the overall behavior must be considered, are modeled with the FEM. However, these coupling methods may encounter certain issues, including wave reflections at the FEM/DEM coupling interface [25,26]. Some authors [20,27] have shown that the use of overlap helps reduce the phenomenon of wave reflection, but the use of overlaped layers significantly increases the computation time compared to methods without overlap [25,26].
It should be highlighted that a difficulty relies in the fact that the use of a coupling requires prior knowledge on the subdomains that would be likely to exhibit crack initiation and propagation. In fact, such information are generally unknown for industrial applications involving complex geometries or multi-directional loads and boundary conditions. To avoid the need for prior knowledge on where cracks would be likely to initiate and propagate, it would be interesting to substitute an initially FEM-meshed region with a DEM region only at the time and the location needed.
Furthermore, since DEM is very costly, using it in some regions from the beginning of the computation, not just when necessary, makes the initial FEM-DEM coupling expensive. An adaptive remeshing strategy would thus be really interesting. However, to the knowledge of the authors, such a strategy has not been proposed yet. This is the motivation of the work presented here. It aims at developing a FEM-DEM remeshing method that allows substituting a FEM region with a DEM region at the instant of the computation and in the area of the computational domain required, to benefit from FEM efficiency as long as possible, and then benefit from the precision of DEM for crack modeling. To achieve this, it seems appropriate to explore coupling methods, field transfer, and dynamic remeshing.

The article is organized as follows. Section 2 presents the features of the time and space discretizations employed in the computational domain. Section 3 proposes the specifications of the dynamic resmeshing strategy. The coupling and field transfer methods employed are respectively presented in Sections 4 and 5. Finally, the methodology proposed is evaluated in Section 6.

2 | DISCRETIZATIONS

In this section, two types of discretizations have been covered: time discretization, which includes the Central Difference (CD) integration scheme, and spatial discretization, which encompasses FEM and DEM.

2.1 | Time discretization

For the structural domain, the temporal integration is carried out using the CD scheme. The objective of this section is to incorporate the coupling method (developed in Section 4) into this numerical scheme. Let us consider a variable time increment

Δt, where Δt^n represents the time step that led to the current configuration $\mathbf{x}^{n+1}$, and Δt^{n+1} represents the next time step:

$$\Delta t^n \equiv t^{n+1} - t^n, \tag{1}$$

$$\Delta t^{n+1} \equiv t^{n+2} - t^{n+1}. \tag{2}$$

It is assumed that the solution is complete, meaning that all discrete quantities are known at time t^n, and we want to find the solution at t^{n+1}. First, an intermediate velocity at the half step is introduced, sometimes referred to as the "velocity precursor" because it depends only on the quantities at t^n, especially on the acceleration $\mathbf{a}^n$, and it is calculated:

$$\mathbf{v}^{n+1/2} = \mathbf{v}^n + (\Delta t^n/2)\mathbf{a}^n. \tag{3}$$

This is the constant velocity that transforms the configuration from n to $n+1$ over the time interval Δt^n. Therefore, the new (that is, current) displacements are given by:

$$\mathbf{u}^{n+1} = \mathbf{u}^n + \Delta t^n \mathbf{v}^{n+1/2}. \tag{4}$$

The positions are then calculated from the displacements as follows:

$$\mathbf{x}^{n+1} = \mathbf{x}^n + \Delta t^n \mathbf{v}^{n+1/2} = \mathbf{x}^0 + \mathbf{u}^{n+1}. \tag{5}$$

Next, the accelerations $\mathbf{a}^{n+1}$ are calculated using the equilibrium equations:

$$\mathbf{a}^{n+1} = \mathscr{M}^{-1}(\mathbf{f}^{ext} - \mathbf{f}^{int})^{n+1}. \tag{6}$$

Finally, the velocities $\mathbf{v}^{n+1}$ are obtained:

$$\mathbf{v}^{n+1} = \mathbf{v}^{n+1/2} + (\Delta t^n/2)\mathbf{a}^{n+1}, \tag{7}$$

where $\mathbf{f}^{ext}$ and $\mathbf{f}^{int}$ are the external and internal forces, defined over the global domain.

2.2 | Spatial discretization

2.2.1 | Finite Element Method

There are numerous methods for continuous spatial simulation that span a wide range of domains and are increasingly prevalent in commercial codes. In this study, we specifically focus on the classical FEM[28].
The FEM is based on a discrete mathematical theory allowing to find an approximate solution of a set of partial differential equation on a continuous compact domain. Within the element, the value of a displacement function u is determined using a polynomial interpolation of the values of displacements at the nodes u_i and elements shape functions N_i:

$$u(x, y, z) \simeq \sum_{i=1}^{n} N_i(x, y, z)\, u_i, \tag{8}$$

where n is the number of nodes. The nodal internal forces are determined from the stress tensor $\boldsymbol{\sigma}$ and the strain-displacement matrix $\mathbf{B}$ in the following form:

$$\mathbf{f}^{int} = \sum_e \int_{V_e} \mathbf{B}^T \boldsymbol{\sigma} \mathrm{dV}, \tag{9}$$

were the summation symbol represents the ordinary assembly operator over all elements e of the mesh, and V_e is the element volume in the current configuration.

2.2.2 | Discrete Element Method

The DEM used in this article is a hybrid method combining the distinct element method[11] and the lattice method[15] developed by André et al.[12]. The medium is discretized by an assembly of particles of various sizes distributed randomly in the domain. The disorderly arrangement is essential to represent the heterogeneous nature that is the source of cracking but also to ensure

the isotropy of the structure. The particles are interconnected with their nearest neighbors through cohesive bonds of the Euler-Bernoulli type[12]. These bonds have a cylindrical shape that can be described by two parameters: the length l_μ and the radius r_μ. There are also two associated mechanical parameters: the Young's modulus E_μ and the Poisson's ratio ν_μ. The microscopic properties, denoted by the index μ, which generally differ from the macroscopic properties, must be calibrated so that the defined microscopic properties allow obtaining the targetted macroscopic behavior.

The configuration shown in Figure 1 allows for a better understanding of the kinematics of discrete elements[29,30]. The cohesive beam is represented by its centerline and is fixed to the centers of the DE O_1 and O_2 located at the ends. The coordinate systems $F_1(O_1, X_1, Y_1, Z_1)$ and $F_2(O_2, X_2, Y_2, Z_2)$ are arranged such that axes X_1 and X_2 are perpendicular to the ends of the cross-section of the beam. Initially, the beams are in a relaxed state (Figure 1a). However, as the DE move and rotate, the cohesive beam undergoes a load, as shown in Figure 1b.

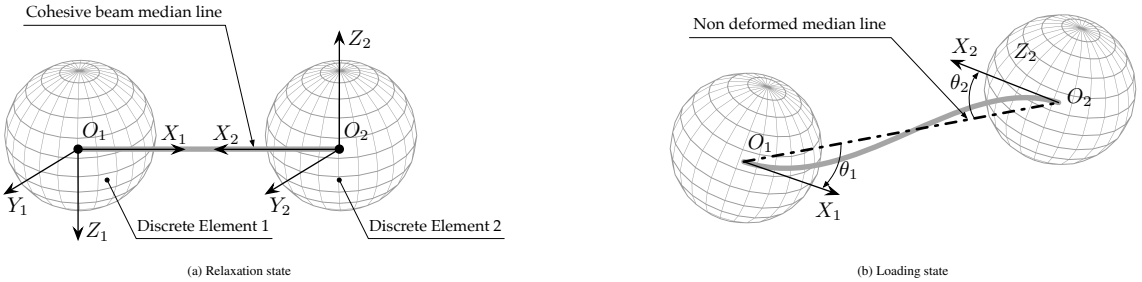

FIGURE 1 Configurations of cohesive beam[12]

In the local coordinate system $F(O, X, Y, Z)$, the arrows at O_1 and O_2 are zero. The bending rotations of the cross-section at O_1 and O_2 are defined as $\theta_1 = (X, X_1)$ and $\theta_2 = -(X, X_2)$, respectively (Figure 1b). By applying the principles of the strength of materials to Euler-Bernoulli beams[29,30], it is possible to calculate the reaction forces and reaction moments acting on DE 1 and 2, according to the following system of equations:

$$\begin{aligned}
\overrightarrow{F_{B/DE1}} &= +E_\mu S_\mu \frac{\Delta l_\mu}{l_\mu}\vec{X} - \frac{6E_\mu I_\mu}{l_\mu^2}\left(\left(\theta_{2z}+\theta_{1z}\right)\vec{Y} + \left(\theta_{2y}+\theta_{1y}\right)\vec{Z}\right),\\
\overrightarrow{F_{B/DE2}} &= -E_\mu S_\mu \frac{\Delta l_\mu}{l_\mu}\vec{X} + \frac{6E_\mu I_\mu}{l_\mu^2}\left(\left(\theta_{2z}+\theta_{1z}\right)\vec{Y} - \left(\theta_{2y}+\theta_{1y}\right)\vec{Z}\right),\\
\overrightarrow{T_{B/DE1}} &= +\frac{G_\mu Io_\mu}{l_\mu}\left(\theta_{2x}-\theta_{1x}\right)\vec{X} - \frac{2E_\mu I_\mu}{l_\mu}\left(\left(\theta_{2y}+2\theta_{1y}\right)\vec{Y} - \left(\theta_{2z}+2\theta_{1z}\right)\vec{Z}\right),\\
\overrightarrow{T_{B/DE2}} &= -\frac{G_\mu Io_\mu}{l_\mu}\left(\theta_{2x}-\theta_{1x}\right)\vec{X} - \frac{2E_\mu I_\mu}{l_\mu}\left(\left(2\theta_{2y}+\theta_{1y}\right)\vec{Y} - \left(2\theta_{2z}+\theta_{1z}\right)\vec{Z}\right),
\end{aligned} \tag{10}$$

with:

- $\overrightarrow{F_{B/DE1}}$ is the reaction force of the beam on DE 1,
- $\overrightarrow{F_{B/DE2}}$ is the reaction force of the beam on DE 2,
- $\overrightarrow{T_{B/DE1}}$ is the reaction moment of the beam on DE 1,
- $\overrightarrow{T_{B/DE2}}$ is the reaction moment of the beam on DE 2,
- l_μ is the initial length of the beam,
- Δl_μ is the elongation of the beam,
- $\overrightarrow{\theta_1}(\theta_{1x}, \theta_{1y}, \theta_{1z})$ is the rotation of the cross-section at point O_1,
- $\overrightarrow{\theta_2}(\theta_{2x}, \theta_{2y}, \theta_{2z})$ is the rotation of the cross-section at point O_2,
- S_μ is the cross-sectional area of the beam,
- Io_μ is the polar moment of inertia of the beam's cross-section,
- I_μ is the moment of inertia of the beam's cross-section about the $\overrightarrow{Y}$ and $\overrightarrow{Z}$ axes.

The main objective of the dynamic remeshing method is to enhance computational efficiency by utilizing the FEM as extensively as possible, both spatially and temporally, due to its cost efficiency compared to the DEM. It involves using the DEM, which is more computationally expensive than FEM, only when necessary, based on a user-defined criterion : the subdomain substitution criterion.

3 | DYNAMIC REMESHING STRATEGY

The different steps leading to the use of the FEM-DEM dynamic remeshing in an initially purely FEM computation are outlined below.

The *first step* involves performing a conventional computation using only FE, as illustrated in Figure 2a. This FEM computation goes on until the iteration preceding the remeshing, in this example (i.e., before the substitution criterion is met), defined by an applied force value equal to $\vec{F}$ (Figure 2b).

The *second step* begins when the predefined substitution criterion for transitioning from the FEM to the DEM is reached. The choice of the type and numerical value associated will be up to user according to his know-how, and is expected to be potentially problem dependent. It could for example be based on criteria such as constraints, strains, energies, etc. The FE that meet this substitution criterion will form one or more subdomains of FE to be replaced. At the current time step, the geometry of these elements defines the boundaries of the DE subdomain to be generated. Once the DEM subdomain generated, the FE to be replaced are removed, and the new DE subdomain takes its place, as presented in Figure 2c.

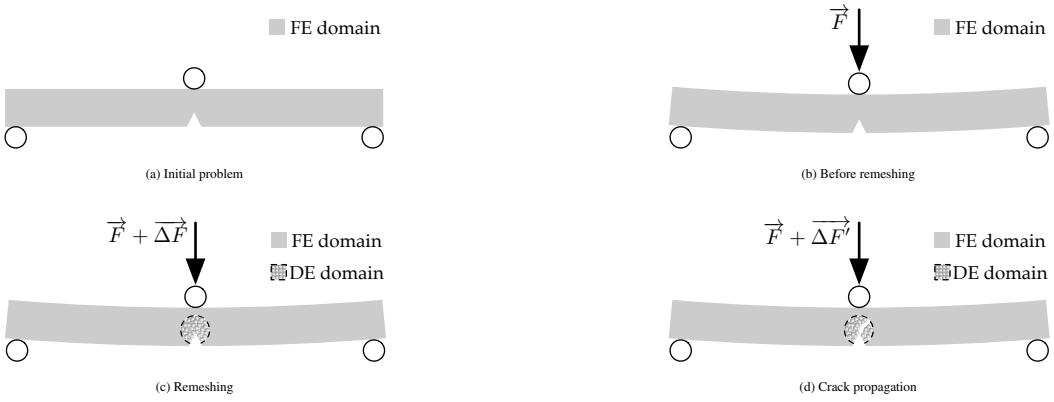

FIGURE 2 Dynamic remeshing strategy

Before removing the FE, the coupling interfaces are determined by identifying the common surfaces with neighboring elements. These surfaces are then used to define the necessary couplings after the substitution of domains. To fill the identified envelop with DE, it is chosen to employ an application dedicated to and validated for this task (instead of developing a new tool). To this end, the "Cooker" tool, distributed along with the GranOO Workbench[30] is employed. It requires closed shell envelops to discretize a considered subdomain with DE. In fact, the coupling surfaces determined previously correspond to the requirements of the application, and are thus provided to it. However, this leads to an insufficient alignment issue between the nodes of DE and the coupling interfaces, as the position of these nodes depends on the radius of associated particles. Instead, this application favors a more regular outer surface. As shown in the Figure 3, the DEM subdomain is generated based on the external boundary.

This configuration results in a misalignment between the coupling interface on the FE side and the DE side because the DE interface is defined by the nodes modeled by the centers of the DE existing at the interface (centers of the DE in light gray, as presented in the Figure 3). This requires the use of a projection technique to achieve a common coupling surface.

During the substitution phase, the dynamic remeshing involves a phase of transitioning from the FEM to the DEM. At this transition point, the fields within the FEM domain are known. However, the DEM subdomain is a "raw" domain imported at this stage. In fact, two cases are envisaged during the computation when substituting a FE subdomain: either the FE subdomain is isolated, or it is neighboring an existing DE subdomain. In the first case an operation to transfer the fields from the FEM

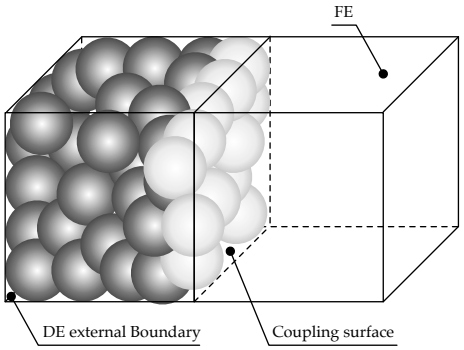

FIGURE 3 Shifted nodes configuration

domain to the DEM must be carried out. In this second case a transfer configuration involves transitioning from a subdomain that combines discrete/finite elements to a subdomain consisting solely of DE, as illustrated in Figure 4. In the second case, there were two possible options for carrying out the substitution: either substituting each DEM subdomain individually or merging adjacent DEM subdomains. Substituting DEM subdomains individually may create preferential planes at the junction of DEM subdomains. To address this, it was decided to always redefine neighboring DEM domains into one.

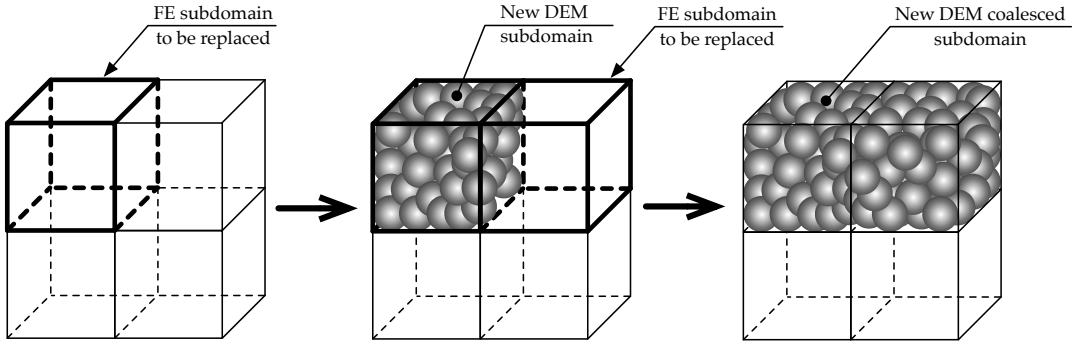

FIGURE 4 Transition from a combined FEM/DEM subdomain to a purely DEM subdomain

Due to the geometric complexity of the generated DEM subdomains, as well as the significant computation time required for calibrating DEM subdomains for each substitution operation, a reference calibration process is initially performed independently of the main computation. This calibration is carried out, once for all, on a simple geometric reference shape to determine the microscopic parameters of the DE within the subdomain. In order to preserve the microscopic behavior of the reference domain, the same average radius of the DE is used in both the reference calibration and the main computation. An organizational chart illustrating the various stages of the dynamic remeshing strategy and the connections between them is shown in the Figure 5.

The *third step* begins after performing the substitution of subdomains. The new configuration is characterized by two distinct subdomains: one domain consisting of FE located outside the area of interest, and one or more DE subdomains in the areas of interest (for example regions of high gradients, where the substitution criterion was met) that happens to be the most loaded region. For a generic subdomain consisting of DE, it is essential to define a crack criterion, which can be based on parameters such as strain, stress, energy, etc. This criterion determines the threshold at which beams must be broken to allow crack propagation. Consequently, the crack pattern is developed by grouping all beams that satisfy the chosen crack criterion, as shown in Figure 2d. The crack propagation pattern is expected to influence the transition from FE to DE of some subdomains in the forthcoming steps of the computation.

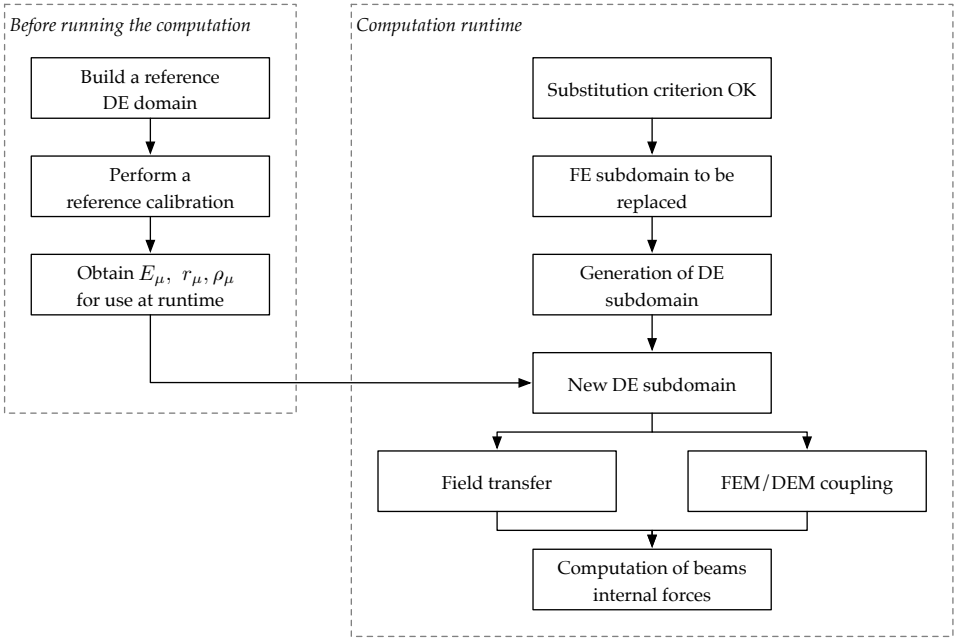

FIGURE 5 Dynamic remeshing flowchart

To successfully implement this strategy, it is necessary to set-up two numerical methods. The first one involves creating a coupling method between the DE and FE subdomains. The second numerical method entails transferring the fields from the existing subdomain to be replaced to the new replacement subdomain.

4 | COUPLING METHOD

During the dynamic remeshing process, coupling is an essential phase to ensure cohesion between the FE subdomains and DE subdomains after transitioning from the FEM subdomain to a combined FEM/DEM subdomain.
The coupling method used[31] is a non-overlapping method based on the principle of cohesion between the two FEM/DEM subdomains. The coupling forces are sought at each computation increment, and a compatibility condition of velocities at the coupling interfaces is ensured through the use of the Lagrange multipliers method. This condition must be satisfied at each computation step by calculating new multipliers. In the context of fast dynamics explicit computations, velocity coupling may be more appropriate than displacement coupling. Indeed, velocity coupling allows for a better consideration of the dynamic response of the system, especially inertia effects.
The formulation of dynamic equilibrium for both finite and discrete subdomains is modified by the inclusion of a coupling force term $\mathbf{f}^c$, which leads to the expression of the following equation of motion:

$$\mathscr{M}\,\mathbf{a} = \mathbf{f}^{ext} - \mathbf{f}^{int} + \mathbf{f}^c. \tag{11}$$

This equation can be rewritten in a way to separate each subdomain:

$$\begin{aligned} m\mathbf{a}_m &= \mathbf{f}^{ext}_m - f^{int}_m + \mathbf{f}^c_m \qquad \text{(DE subdomain)},\\ M\mathbf{a}_M &= \mathbf{f}^{ext}_M - f^{int}_M + \mathbf{f}^c_M \qquad \text{(FE subdomain)}. \end{aligned} \tag{12}$$

4.1 | Treatment of essential boundary conditions

For a coupled domain, the force $\mathbf{f}^c$ acts on all components of the interface and is calculated by imposing that all components of the velocities of the subdomains on either side of the coupling interface are equal, in order to prevent detachment, sliding,

or interpenetration. Let $v_M(X)$ and $v_m(X)$ be the respective velocities at the interfaces Γ_M and Γ_m, defined at the same point X (Figure 6), the compatibility condition (kinematic, on velocities) is written as:

$$\mathbf{v}_M(X)\begin{pmatrix}\mathbf{v}_{Mx}\\ \mathbf{v}_{My}\\ \mathbf{v}_{Mz}\end{pmatrix} = \mathbf{v}_m(X)\begin{pmatrix}\mathbf{v}_{mx}\\ \mathbf{v}_{my}\\ \mathbf{v}_{mz}\end{pmatrix}. \tag{13}$$

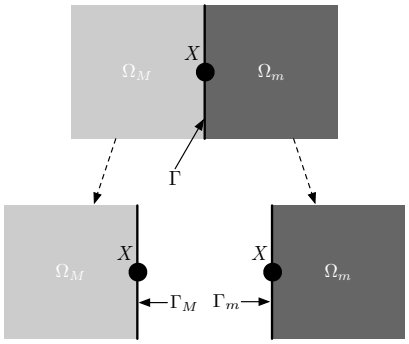

FIGURE 6 Domain Decomposition

The condition presented in Equation 13 can be written in a generalized form to account for all degrees of translational freedom existing within the coupling interface, based on a coupling matrix $\mathbf{C}$ and a velocity vector $\mathbf{b}$ that equals a null vector in the case where $\forall X \in \Gamma$, $v_M(X) = v_m(X)$. According to the CD time integration scheme detailed in Section 2.1, the velocities are computed at mid time steps. The new generalized matrix system can be written as follows:

$$\mathbf{C}^{n+1}\mathbf{v}^{n+3/2} = \mathbf{b}^{n+1}, \tag{14}$$

where $\mathbf{v}$ and $\mathbf{C}$ are composite quantities, which can be expressed in the following form:

$$\mathbf{v} = \begin{pmatrix}\mathbf{v}_M\\ \mathbf{v}_m\end{pmatrix}, \quad \mathbf{C} = \begin{pmatrix}\mathbf{C}_M & \mathbf{C}_m\end{pmatrix}. \tag{15}$$

Equation 14 can then be decomposed as follows:

$$\mathbf{C}^{n+1}\begin{pmatrix}\mathbf{v}_M\\ \mathbf{v}_m\end{pmatrix}^{n+3/2} = \begin{pmatrix}\mathbf{C}_M^{n+1} & \mathbf{C}_m^{n+1}\end{pmatrix}\begin{pmatrix}\mathbf{v}_M\\ \mathbf{v}_m\end{pmatrix}^{n+3/2} = \mathbf{C}_M^{n+1}\mathbf{v}_M^{n+3/2} + \mathbf{C}_m^{n+1}\mathbf{v}_m^{n+3/2} = \mathbf{b}^{n+1}. \tag{16}$$

In order to introduce the constraints (Equation 14) into the equilibrium equation (Equation 11), the method of Lagrange multipliers is employed. The unknown coupling forces, which can also be interpreted as cohesion forces, can be expressed as follows:

$$\mathbf{f}^c = \mathbf{C}^T\Lambda, \tag{17}$$

where Λ is the vector of Lagrange multipliers. By combining Equation 11 and Equation 17, the new form of the motion equation at an increment $n+1$ is written as follows:

$$\mathscr{M}^{n+1}\mathbf{a}^{n+1} = \mathbf{f}^{ext(n+1)} - \mathbf{f}^{int(n+1)} + \mathbf{C}^{n+1^T}\Lambda^{n+1}. \tag{18}$$

The matrices $\mathscr{M}$ and $\mathbf{C}$ are initially defined matrices, which means that for all $n \in \mathbb{N}$, $\mathscr{M}^n = \mathscr{M}$ and $\mathbf{C}^n = \mathbf{C}$. By multiplying both sides of Equation 18 by $\mathbf{C}\mathscr{M}^{-1}$:

$$\mathbf{C}\mathbf{a}^{n+1} = \mathbf{C}\mathscr{M}^{-1}(\mathbf{f}^{ext(n+1)} - \mathbf{f}^{int(n+1)}) + \mathbf{C}\mathscr{M}^{-1}\mathbf{C}^T\Lambda^{n+1}. \tag{19}$$

Finally, according to Equation 19, the Lagrange multipliers vector can be expressed in the following form:

$$\Lambda^{n+1} = \mathbf{L}^{-1}.\mathbf{W}^{n+1}, \tag{20}$$

where it can be identified, by comparing equations 19 and 20, that the expressions of $\mathbf{L}$ and $\mathbf{W}$ have been simply posed such that:

$$\mathbf{L} = \mathbf{C}\mathscr{M}^{-1}\mathbf{C}^T, \tag{21}$$

$$\mathbf{W}^{n+1} = \mathbf{C}\mathbf{a}^{n+1} - \mathbf{C}\mathscr{M}^{-1}(\mathbf{f}^{ext(n+1)} - \mathbf{f}^{int(n+1)}). \tag{22}$$

The constraint of Equation 20 can be used simultaneously with the CD time integration scheme. Starting from Equations 3 and 7, the velocities at the interfaces can be expressed, while adhering to the CD temporal discretization, the quantity $\mathbf{W}$ presented in Equation 22 can be rewritten in the following form:

$$\mathbf{W}^{n+1} = \frac{2}{\Delta t^n + \Delta t^{n+1}} \left(\mathbf{b}^{n+1} - \mathbf{C}\mathbf{v}^{n+1/2}\right) - \mathbf{C}\mathscr{M}^{-1}(\mathbf{f}^{ext(n+1)} - \mathbf{f}^{int(n+1)}). \tag{23}$$

4.2 | Projection technique

A projection technique was used to determine the coupling matrix. This technique is based on the principle of projecting a node from the discrete interface Γ_m onto the corresponding facet (represented by a 2D element) of the FE associated with Γ_M, as shown in Figure 7.

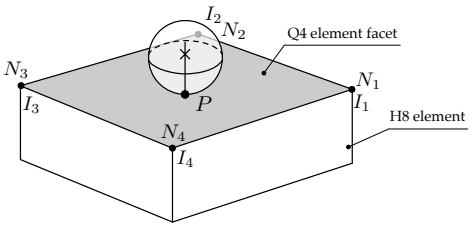

FIGURE 7 The projection of a node from the discrete interface

For example, for an H8 FE (a first-order 3D hexahedral element with 8 nodes), using the shape functions N_i of the associated Q4 element (a four-node first-order quadrilateral element) with nodes I_i and point P, the coupling matrix in the case of Figure 7 can be written as follows:

$$\mathbf{C} = \begin{pmatrix} N_1^{Q4}\chi_1^3 & N_2^{Q4}\chi_1^3 & N_3^{Q4}\chi_1^3 & N_4^{Q4}\chi_1^3 & -\chi_1^3 \\ N_1^{Q4}\chi_2^3 & N_2^{Q4}\chi_2^3 & N_3^{Q4}\chi_2^3 & N_4^{Q4}\chi_2^3 & -\chi_2^3 \\ N_1^{Q4}\chi_3^3 & N_2^{Q4}\chi_3^3 & N_3^{Q4}\chi_3^3 & N_4^{Q4}\chi_3^3 & -\chi_3^3 \end{pmatrix}, \tag{24}$$

with the vector χ_p^n being a vector of dimension $(1, n)$ consisting entirely of zeros except for the component at position p, which is equal to 1. N^{Q4} is a matrix of shape functions defined as follows:

$$N^{Q4} = \left(N_1^{Q4}(\xi,\eta)\ N_2^{Q4}(\xi,\eta)\ N_3^{Q4}(\xi,\eta)\ N_4^{Q4}(\xi,\eta)\right). \tag{25}$$

5 | FIELD TRANSFER METHOD

Dynamic remeshing involves two types of information transfers. The first type consists of exchanging of spatial information between existing domains, such as in the coupling presented in the previous section. The second type of transfer is temporal, and it involves the procedure for transporting data from the initial mesh to the new mesh during the transition from one subdomain to

another. This data can include physical quantities such as temperature, pressure, velocity, etc., which have been computed based on the initial mesh. The primary objective is to preserve relevant information as much as possible while adapting it to the new mesh configuration.

5.1 | Transition from a purely FEM subdomain to a purely DEM subdomain

The kinematic variables of DE particles at the time of transfer (at time t_{nt}) are obtained through interpolation of nodal (FE) values. The displacements and velocities are calculated using interpolation that utilizes the shape functions of FE and the displacements of nodes at t_{nt} and t_{nt-1}. The displacements and velocities of a DE particle are calculated as follows (Figure 8):

$$U_d^{t_{nt}} = N(X_d)U_F^{t_{nt}}, \tag{26}$$

$$V_d^{t_{nt-\frac{1}{2}}} = N(X_d)\frac{(U_F^{t_{nt}} - U_F^{t_{nt-1}})}{(t_{nt} - t_{nt-1})}, \tag{27}$$

with U_d and V_d being the displacement and velocity of particle d, U_F and V_F being the displacement and velocity of the FE that encompasses d, and N being the matrix of shape functions of the FE.

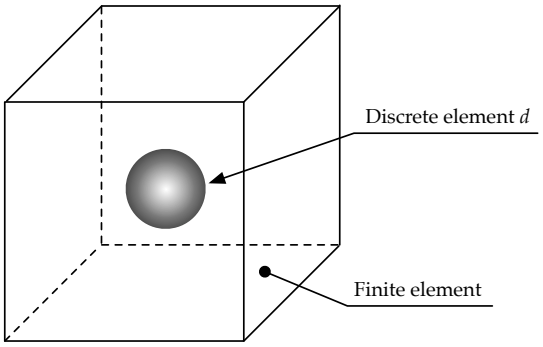

FIGURE 8 Displacement transfer

DE have three additional degrees of freedom for rotation compared to solid FE. The transfer of these rotations is based on the infinitesimal deformations of the "container" FE. For example, the rotation of a point A in the (x, y) plane around z–axis, as shown in Figure 9, is determined using a decomposition of the displacements along the two axes x (u_x) and y (u_y) in a first-order Taylor series (Equation 28).

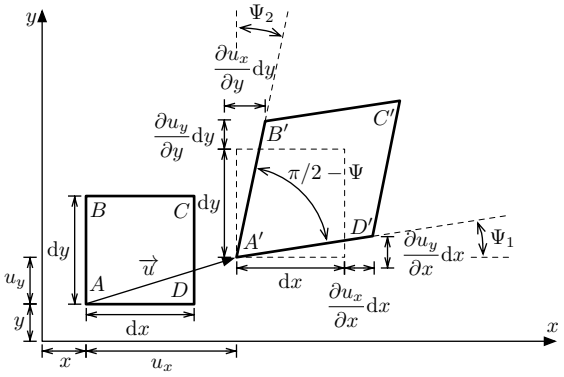

FIGURE 9 Displacement decomposition

$$\begin{aligned} u_x &= u_x^0 + \frac{\partial u_x}{\partial x}dx + \frac{\partial u_x}{\partial y}dy, \\ u_y &= u_y^0 + \frac{\partial u_y}{\partial x}dx + \frac{\partial u_y}{\partial y}dy. \end{aligned} \tag{28}$$

The angle variations can be calculated as follows:

$$\begin{aligned} \tan\Psi_1 &= \frac{\frac{\partial \mathrm{u_x}}{\partial \mathrm{y}} \cdot dy}{\partial \mathrm{y}} = \frac{\partial \mathrm{u_x}}{\partial \mathrm{y}}, \\ \tan\Psi_2 &= \frac{\frac{\partial \mathrm{u_y}}{\partial \mathrm{x}} \cdot dx}{\partial \mathrm{x}} = \frac{\partial \mathrm{u_y}}{\partial \mathrm{x}}. \end{aligned} \tag{29}$$

In the context of the small perturbation assumption, or in other words, for small values of Ψ_1 and Ψ_2, the variations can be rewritten as follows:

$$\begin{aligned} \tan\Psi_1 &= \Psi_1 \\ \tan\Psi_2 &= \Psi_2 \end{aligned} \tag{30}$$

The rotation θ_z of point A, as illustrated in Figure 10, can be determined as a function of Ψ_1 and Ψ_2:

$$\theta_z = \Psi_1 + \Psi_2 = \frac{\partial \mathrm{u_y}}{\partial \mathrm{x}} - \frac{\partial \mathrm{u_x}}{\partial \mathrm{y}}. \tag{31}$$

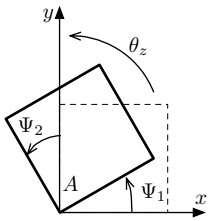

FIGURE 10 Rotation of point A

The deformation can also be decomposed into a symmetric part and an antisymmetric part:

$$\nabla \boldsymbol{u} = \underbrace{\frac{1}{2}\left(\nabla \boldsymbol{u} + \nabla \boldsymbol{u}^T\right)}_{\varepsilon} + \underbrace{\frac{1}{2}\left(\nabla \boldsymbol{u} - \nabla \boldsymbol{u}^T\right)}_{\omega}. \tag{32}$$

In the 2D case, the strain tensor ε and the infinitesimal rotation tensor ω are written as:

$$\varepsilon = \frac{1}{2}\begin{vmatrix} \frac{\partial u_x}{\partial x} + \frac{\partial u_x}{\partial x} & \frac{\partial u_y}{\partial x} + \frac{\partial u_x}{\partial y} \\ \frac{\partial u_y}{\partial x} + \frac{\partial u_x}{\partial y} & \frac{\partial u}{\partial y} + \frac{\partial u}{\partial y} \end{vmatrix}, \tag{33}$$

$$\omega = \frac{1}{2}\begin{vmatrix} 0 & \frac{\partial u_y}{\partial x} - \frac{\partial u_x}{\partial y} \\ -\frac{\partial u_y}{\partial x} + \frac{\partial u_x}{\partial y} & 0 \end{vmatrix}. \tag{34}$$

The rotation θ_z can be rewritten as a function of ω:

$$\theta_z = \Psi_1 + \Psi_2 = 2\omega_{xy} = -2\omega_{yx}. \tag{35}$$

This methodology for calculating rotations can be extended to the general 3D case. The infinitesimal rotation tensor (3D) is written as:

$$\omega = \begin{bmatrix} 0 & \omega_{xy} & \omega_{xz} \\ \omega_{yx} & 0 & \omega_{yz} \\ \omega_{zx} & \omega_{zy} & 0 \end{bmatrix} = \begin{bmatrix} 0 & \frac{1}{2}\left(\frac{\partial u_y}{\partial x} - \frac{\partial u_x}{\partial y}\right) & \frac{1}{2}\left(\frac{\partial u_z}{\partial x} - \frac{\partial u_x}{\partial z}\right) \\ \frac{1}{2}\left(-\frac{\partial u_y}{\partial x} + \frac{\partial u_x}{\partial y}\right) & 0 & \frac{1}{2}\left(\frac{\partial u_z}{\partial y} - \frac{\partial u_y}{\partial z}\right) \\ \frac{1}{2}\left(-\frac{\partial u_z}{\partial x} + \frac{\partial u_x}{\partial z}\right) & \frac{1}{2}\left(-\frac{\partial u_z}{\partial y} + \frac{\partial u_y}{\partial z}\right) & 0 \end{bmatrix}. \tag{36}$$

Finally, the rotations θ_x, θ_y, and θ_z around the x–, y–, and z–axes, respectively, are obtained as:

$$\begin{bmatrix} \theta_x \\ \theta_y \\ \theta_z \end{bmatrix} = \begin{bmatrix} 2\omega_{yz} \\ 2\omega_{xz} \\ 2\omega_{xy} \end{bmatrix}. \tag{37}$$

5.2 | Transition from a combined FEM/DEM subdomain to a purely DEM subdomain

The interpolation techniques mentioned earlier are not suitable for the discontinuous nature of the DE domain. To adapt the interpolation method to a DE domain, it may be wise to introduce an intermediate step that allows for the creation of a FE mesh from the nodes of the DE. In this perspective, one possible approach is to use the least squares technique to determine all displacements from the old DE subdomains to the new one. However, this method has several disadvantages, such as the high computational time cost associated with matrice inversions, as well as choosing the interpolation order. Indeed, with a large number of transfers, the order of displacement interpolation in the FE is no longer preserved in the DE subdomain, which can also lead to discontinuity issues with neighboring FE.

On the other hand, the piecewise interpolation approach could be the solution to these problems. It allows for maintaining a fixed interpolation order using reduced-size or even precomputed interpolation matrices.

To perform this piecewise interpolation, the Delaunay triangulation technique[32,33] (or tetrahedralization in 3D) was employed to create a tetrahedral mesh. The vertices of this mesh are constructed from the positions of the particles, as illustrated in Figure 11 for 2D case.

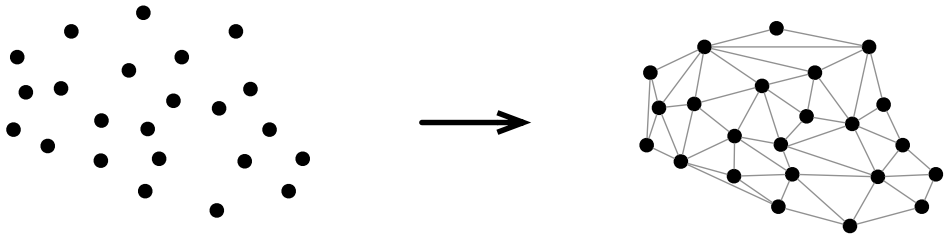

FIGURE 11 Triangular mesh generation (for field interpolation)[34]

Once we have identified the connections and facets of the linear tetrahedra, the next step is to apply a tetrahedral FE (T4) to each geometric shape. Creating a FE mesh allows us to utilize the interpolation method described earlier, using the specific shape functions of the generated T4 element.

At this stage, the transition is made from FEM to DEM rather than from DEM to DEM, thanks to the use of Delaunay triangulation. Therefore, it is sufficient to import the new DEM domain and to apply in a final step as presented in Section 5.1 that enables the transition from a FEM subdomain to a DEM one.

5.3 | Compatibility between coupling method and field transfer method

The local study of velocity continuity at the coupling interfaces, using the field transfer technique presented, reveals that velocities are not continuous when crossing from one side of the interface to the other.

The objective of this section is to propose a method to adjust the displacement fields to ensure velocity continuity. This also involves adjusting the velocity fields accordingly.

The challenge is to adapt the transferred displacements to the geometric position considered by the coupling (Figure 12b), while preserving the overall behavior of the real geometric positions (Figure 12a). In other words, the modifications to the displacement fields should not alter internal forces in the beams to maintain the same mechanical behavior between the replaced subdomain and the replacing subdomain.

Due to mismatching positions, the interface fields were reconstructed (Figure 13a). The global stiffness matrix K^* is defined as the result of the domain mismatch correction. The terms F^* and U^* represent, respectively, the displacements and internal

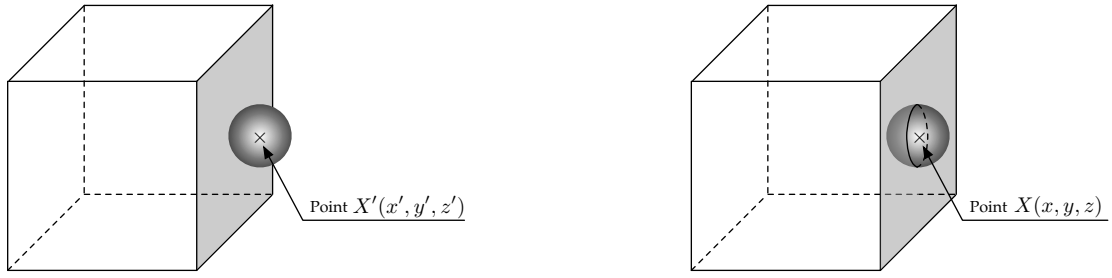

(a) Real geometric position

(b) Position considered by the coupling

FIGURE 12 Geometric position configurations

forces associated with this configuration, such as:

$$F^* = K^* U^*. \tag{38}$$

For the real configuration (Figure 13b), we similarly define the global stiffness matrix K. U^t represents the displacements transferred to the actual geometric position, while F^t represents the associated internal forces, such as:

$$F^t = KU^t. \tag{39}$$

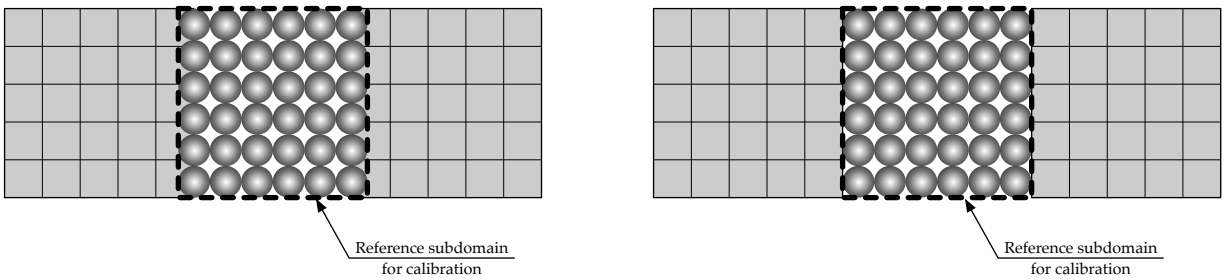

(a) Virtual DE subdomain configuration

(b) Real DE subdomain configuration

FIGURE 13 Virtual and real DE subdomain configurations

The vector U_c represents the displacements of the particles present at the coupling interface. These displacements are calculated using the projection technique presented, which essentially involves interpolating the displacements at the FE nodes using the shape functions of the 2D element constructed by the facet that coincides with the coupling interface. This vector does not depend on the type of configuration, whether it is real or virtual.
The vector can be divided into two parts: the displacement of the particles at the interface, represented by U_c, and the rest of the displacements, represented by U_r^*:

$$U^* = \begin{bmatrix} U_r^* \\ U_c \end{bmatrix}. \tag{40}$$

The requirement for having identical internal forces for both configurations can be formulated as follows:

$$F^t = F^* = KU^t = K^* U^*. \tag{41}$$

The current objective is to determine the displacements U^* appearing in Equation 41, while ensuring equality of internal forces. These displacements are corrected to ensure displacement continuity and, consequently, velocity continuity at the interface. Since the forces F^t are known, the expression for U^* can be simplified as follows:

$$F^t = K^* U^*. \tag{42}$$

In order to make this system invertible, an additional condition needs to be imposed during the resolution. This condition can be enforced by using the known displacements U_c.
Let F_r^t represent the forces associated with the degree of freedom U_r^*. The stiffness matrix can be decomposed as follows:

$$K^* = \begin{bmatrix} K_{r1}^* & K_{c1}^* \\ K_{r2}^* & K_{c2}^* \end{bmatrix}. \tag{43}$$

The new system is expressed as follows:

$$\begin{bmatrix} K_{r1}^* & K_{c1}^* \end{bmatrix} . \begin{bmatrix} U_r^* \\ U_c \end{bmatrix} = F_r^t. \tag{44}$$

Developping system 44:

$$K_{r1}^* . U_r^* = F_r^t - K_{c1}^* . U_c. \tag{45}$$

Finally, the displacements are obtained as follows:

$$U_r^* = (K_{r1}^*)^{-1} . (F_r^t - K_{c1}^* . U_c). \tag{46}$$

6 | NUMERICAL EXAMPLES

The developments of the previous sections, as well as the FEM and DEM frameworks, have been implemented in an in-house program written in Matlab[35]. This program has been chosen for simplicity of development purposes, and explains the (high) computation times given for each numerical exemples, compared to what could be obtained using compiled code.

Three test cases are simulated in this section. The first example is a simple tensile test case that allows us to validate the coupling only. The second one allows us to observe mesh evolution, crack propagation, and assess the consistency between the two. The third example involves the application of dynamic remeshing in a Kalthoff test case, and the results will be validated by comparing the crack propagation angle with experimental data from the literature.

6.1 | Coupling evaluation test case

A simple test case is first performed to evaluate the coupling method only, i.e. the meshes defined remain identical to their initial definition during the whole computation. The specimen is 0.06 m long and features a square cross section with 0.01 m sides. It remains elastic during the whole computation. This model is divided into two domains (DE and FE), of equal length (0.03 m). The coupling is defined at the interface $z = 0.03$ (see Figure 14) using the Lagrange multipliers coupling described in Section 4.

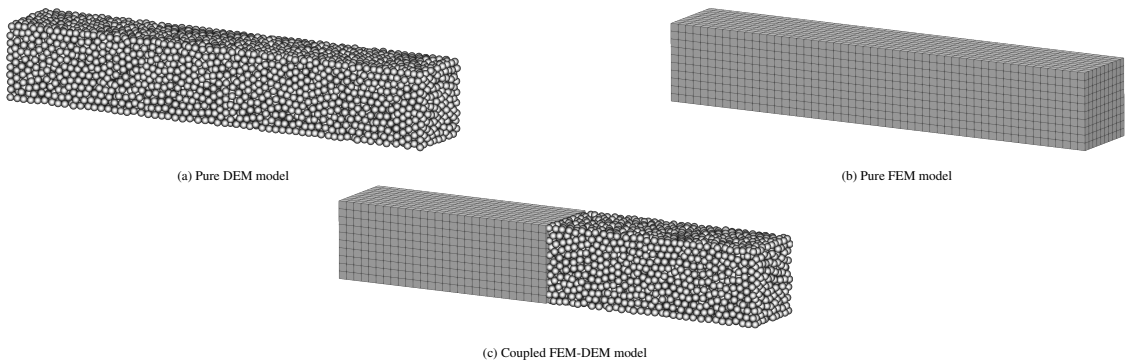

(a) Pure DEM model

(b) Pure FEM model

(c) Coupled FEM-DEM model

FIGURE 14 Models used for the evaluation of the coupling method

A calibration of the discrete subdomain was carried out to determine the microscopic parameters to be applied to the discrete elements based on macroscopic material properties. The discrete subdomain is comprised of 4007 elements assembled by 11571 beams. The geometrical and material properties of both subdomains are presented in Tables 1 and 2 below:

	Elements	DE average radius (m)	Beams	Beams radius (m)
DEM	4007	4.8359×10^{-4}	11571	1.6×10^{-4}
FEM	2800	–	–	–

TABLE 1 Mesh characteristics

	Young's modulus (Pa)	Poisson's ratio	Density (kg m^{-3})
DEM	5.16×10^{12}	0.3	1.25×10^{4}
FEM	2.00×10^{11}	0.3	8000

TABLE 2 DEM microscopic and FEM macroscopic material properties

The results obtained are compared to that of two reference models, made exclusively of either DE or FE (Figure 14). Note that the discretization steps are the same in the three models, which leads to 7966 discrete elements and 23203 beams for the DEM model, and 5600 elements for the FEM model.

Both the global behavior (across the entire domain) and the local behavior (at the coupling interface level) are evaluated. At the global scale, the reaction force time histories are evaluated. At the local scale, the displacement fields at the coupling interface Γ on the FEM side Γ_M and on the DEM side Γ_m were respectively compared to verify if kinematic continuity was well maintained. Two displacements, u_m^* and u_M^*, are associated with the virtual nodes X_m^* and X_M^*, respectively. These two nodes are defined by the intersection of Γ_m and Γ_M with the centerline of the specimen, as illustrated in Figure 15.

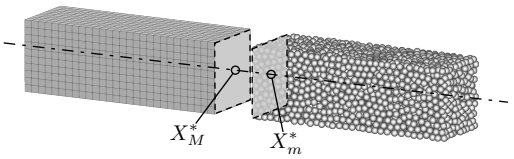

FIGURE 15 Description of local post-treatment

The boundary conditions applied correspond to that of a simple tensile test case. The specimen is clamped at the left end (Figure 16a), while at the right end, it is subjected to a boundary condition of sinusoidal displacement type that evolves over time, as shown in Figure 16b.

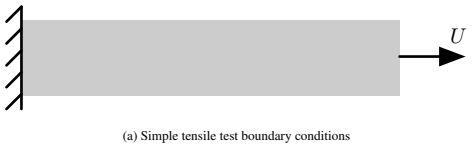

(a) Simple tensile test boundary conditions

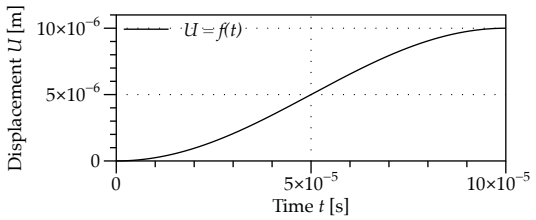

(b) Applied displacement boundary condition

FIGURE 16 Description of the simple tensile test

Figure 17 shows that the coupled model produces a reaction force over time that lies between that of the FEM and DEM reference models. This is a reasuring and somehow intuitive result.

Quantitatively, the coupled FEM-DEM model exhibits a small deviation from both reference models, with a maximum difference of the order of 1.5% with the FEM model and 3.5% with the DEM model. The difference between the FEM and DEM reference solutions can be explained by imperfect calibration between microscopic and macroscopic properties, as well as a non-uniform distribution of masses in DEM, leading to varying levels of inertia effects across different parts of the structure.

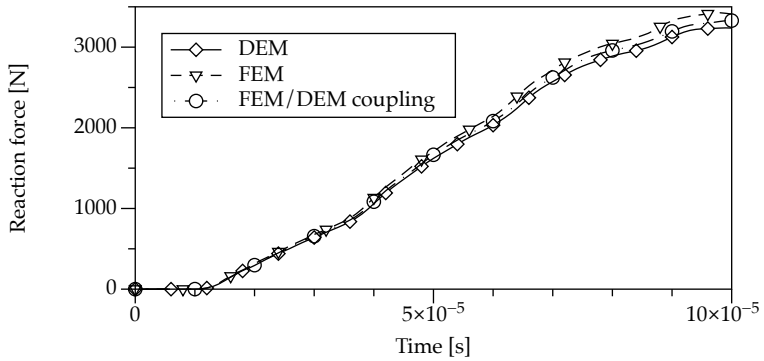

FIGURE 17 Reaction force time histories for DEM, FEM, and coupled FEM/DEM models.

To quantify the vector quantities u_m^* and u_M^*, the time histories of u_m^* and u_M^* are presented in Figure 18. It shows that the displacements on both sides of the coupling interface (FEM side and DEM side) are nearly identical, with a very low relative error, of the order of 0.0039%. This confirms the kinematic continuity at the coupling interface.

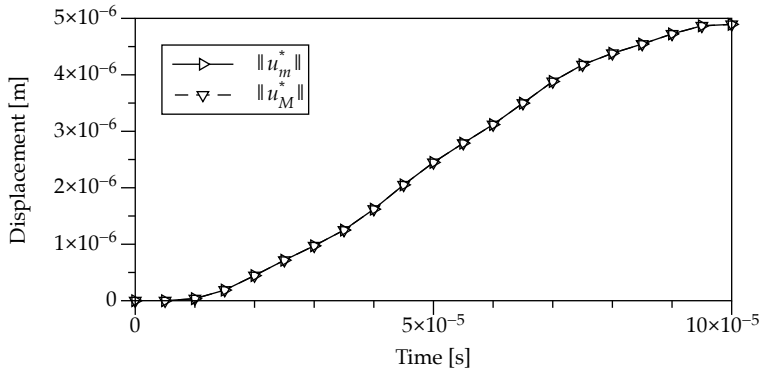

FIGURE 18 Displacement time history for the two post-treatment nodes

6.2 | 6.2 Dynamic remeshing evaluation test case

6.2.1 | Test case definition

This test was conducted on a specimen subjected to uniaxial tension by applying a displacement. The geometry of the specimen promotes crack propagation at the center (Figure 19), and in this context, the crack pattern must be perpendicular to the loading direction. The microscopic parameters of the DE subdomain and the macroscopic mechanical properties of the FE are presented in Table 3. The tests were conducted on a specimen with dimensions of 3 m in length, 1 m in width, and 0.1 m in thickness.

TABLE 3 Macroscopic parameters (FEM) and microscopic parameters (DEM)

	Young's modulus (Pa)	Poisson's ratio	Density (kg m^{-3})	Beam radius (m)
Micro	9.92×10^{12}	0.3	automatic	0.0026
Macro	2.00×10^{11}	0.3	8000	–

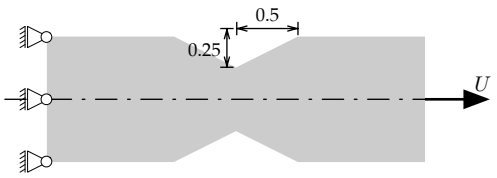

(a) Notched specimen geometry

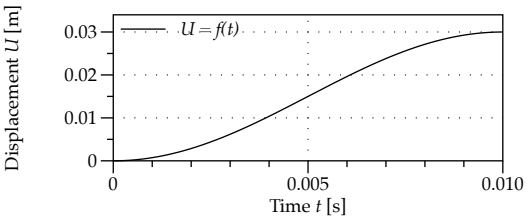

(b) Applied displacement boundary condition

FIGURE 19 Description of the notched tensile test

The failure criterion used in the beams is based on the maximum axial strain and can be written in the following form:

$$\frac{l - l_0}{l_0} > 0.01, \tag{47}$$

with l and l_0 representing the current and initial lengths of the beam in question. The FE substitution criterion is based on the maximum strain and can be written in the following form:

$$\max(\varepsilon) > 0.008. \tag{48}$$

6.2.2 | Numerical results

The results of the mesh evolution and crack propagation at three time instants, $t = 0.0047$ s, $t = 0.005$ s, and $t = 0.0064$ s, are presented in Figure 20. The model was initially constructed entirely from FE (Figure 20a). At time $t = 0.0047$ s, a first remeshing operation was performed. After this remeshing, crack initiation appeared, as illustrated in Figure 20b. This cracking propagated in the central part of the specimen until it reached the FE area, which required a second remeshing operation at $t = 0.005$ s (Figure 20c). The cracks then propagated in two directions, extending within the new subdomain of DE until they joined (Figure 20d). The initial configuration was built with 182 FEs, and at the end of the simulation, the final configuration consisted of 157 EFs and 3115 DEs. The FEM computation time was 51 min, while the coupled FEM-DEM computation time was 6 h 28 min.

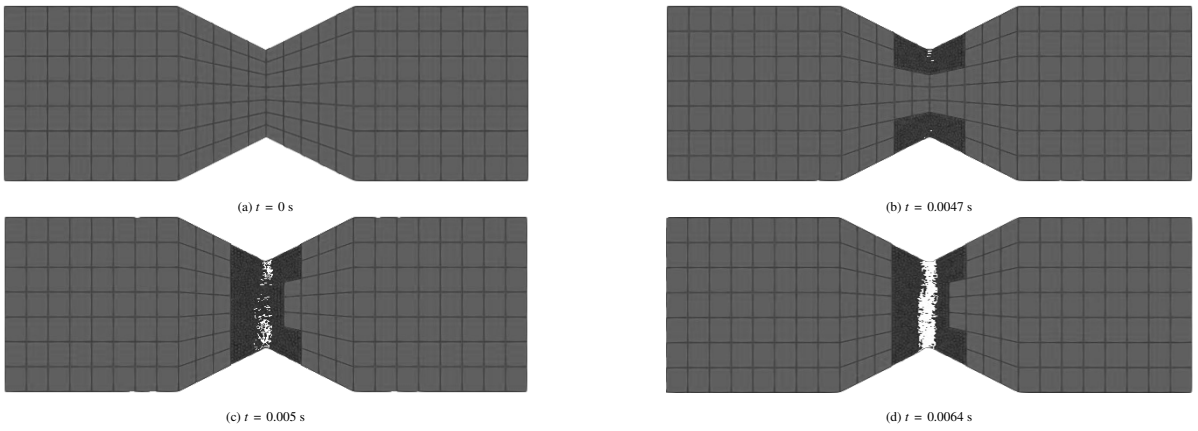

(a) $t = 0$ s (b) $t = 0.0047$ s

(c) $t = 0.005$ s (d) $t = 0.0064$ s

FIGURE 20 Mesh evolution and crack propagation

The asymmetric distribution of DE within the subdomains results in an asymmetry in the crack propagation pattern, leading to an asymmetry in the substitution of subdomains. This feature of DE offers a significant advantage for this method, as it allows for the creation of weak zones in the structure, similar to the presence of real imperfections in materials. These weak zones provide a favorable site for crack initiation, eliminating the need for pre-cracking, unlike crack simulation with continuous methods.

A comparison of computation times was conducted using the same modeling for two scenarios: the first employing the FEM-DEM remeshing method, while the second only used the DEM. This analysis revealed a significant difference between the two approaches, with remeshing computations are estimated to be 26.7 times faster, thereby demonstrating the efficiency and cost-effectiveness of using the FEM-DEM remeshing method.

6.3 | Kalthoff and Winkler's experiment

The study conducted by Kalthoff and Winkler[36,1] involved subjecting a rectangular specimen with two identical initial notches parallel to the impact of a cylindrical projectile (Figure 21). Depending on the applied load velocity, the material type, or temperature, various modes of fracture occur. At relatively low velocities, the experimental results indicate a fracture mode oriented as Mode II, characterized by an average propagation angle of about 70 degrees relative to the initial notch direction.

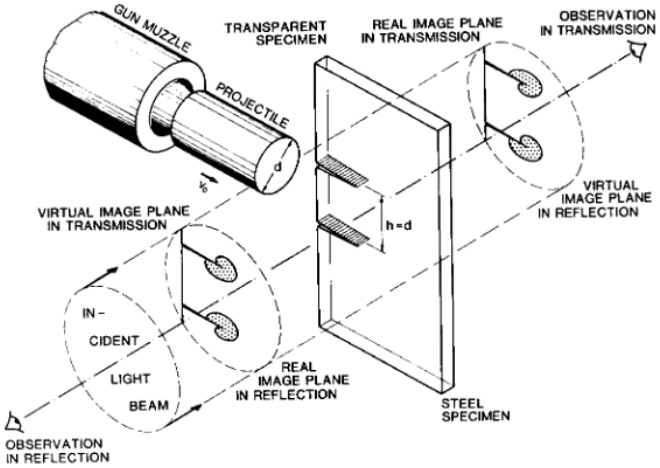

FIGURE 21 Kalthoff experiment[36,1]

The goal here is to compare the results of this experiment with those obtained using the developed remeshing method. The modeling was carried out using the geometry of the specimen presented in Figure 22a. Only half of the specimen is modeled due to the symmetry of the problem. The impact is simulated by imposing a velocity V_0 on the left side of the specimen, which contains a pre-crack, as illustrated in Figure 22b .

The geometric properties of the model and initial conditions are given in Table 4.

TABLE 4 Geometry and initial condition

Parameter	l	h	t	a	V_0
Value	100 mm	200 mm	9 mm	50 mm	10 m s^{-1}

The material represents high-strength brittle martensitic steel 18Ni1900, which is the material used in the experiments. The material properties are as follows: $E = 190$ GPa, $\nu = 0.3$, $\rho = 8000$ kg m^{-3}. To model crack initiation, a critical strain ϵ_f has been used, with $\epsilon_f = 4 \times 10^{-3}$.
The failure criterion used in the beams is based on the maximum axial strain and can be written in the following form:

$$\frac{l - l_0}{l_0} > 4 \times 10^{-3}, \tag{49}$$

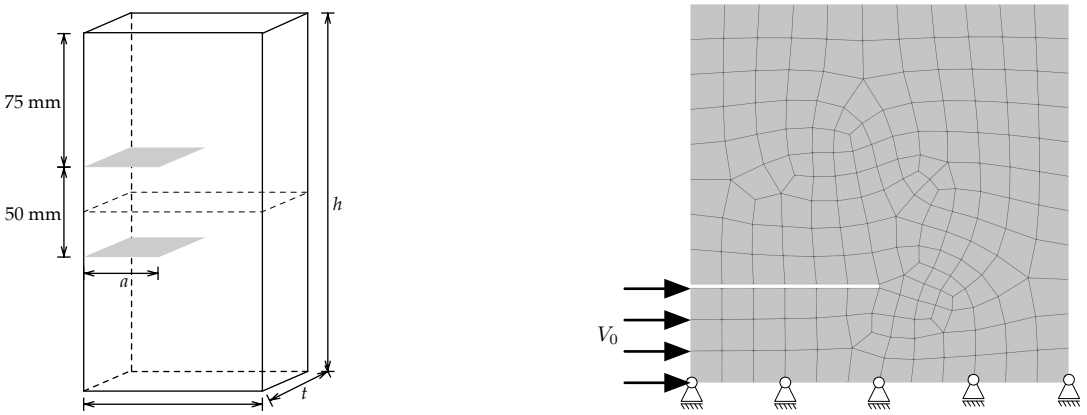

(a) Specimen geometry [37]

(b) Simplified problem

FIGURE 22 Modeling the Kalthoff experiment

with l and l_0 representing the current and initial lengths of the beam in question. The FE substitution criterion is based on the maximum strain and can be written in the following form:

$$\max(\varepsilon) > 3 \times 10^{-3}. \tag{50}$$

The simulation results show an angle of 66° (Figure 23) between the pre-crack and the crack propagation path, which is consistent with experimental observations, as illustrated in Figure 24. The initial configuration was built with 174 FEs, and at the end of the simulation, the final configuration consisted of 164 EFs and 4220 DEs. The FEM computation time was 1 h 7 , while the DEM computation time was 20 h 4 min.

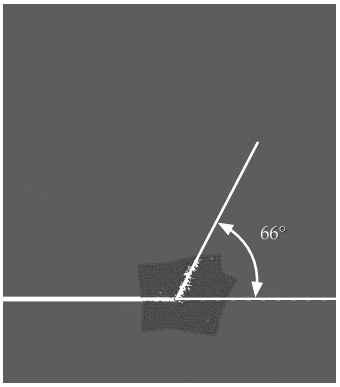

FIGURE 23 Crack path angle

7 | DISCUSSION

7.1 | Spurious waves at the coupling interface

Spurious wave reflections are likely to occur at the coupling interface between sub-domains. This kind of phenomenon occurs not only when coupling FEM and DEM discretized sub-domains [25,26,38], but quite generally when coupling different discretizations for which the sub-domain discretization steps also vary. Indeed, such spurious reflections have for example been observed when performing atomic-to-continuum [39], FEM to peridynamic [40], DEM to Natural Element Method (NEM) [41], DEM to Boundary Element Method (BEM) [42] couplings, to cite only a few examples.

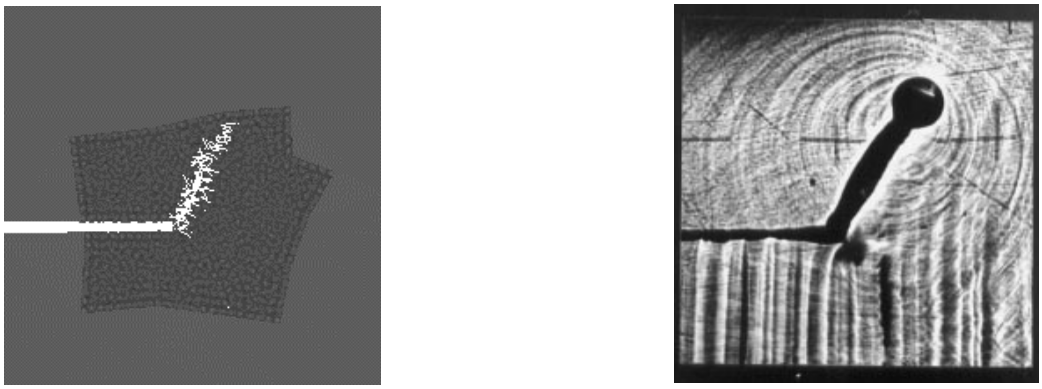

(a) Simulation result

(b) Experimental result [36,1]

FIGURE 24 Comparison between the experiment and the simulation

To avoid spurious wave reflections, a first possibility would be the use of damped time-integration schemes in order to filter out spurious high-frequency components of the response. A quite exhaustive review of such time-integration schemes was proposed by Fung [43]. Some authors also proposed the use of time or spatial filtering [44].

To avoid any additional filtering or damping, many authors employ overlapping methods such as Arlequin [45]. However, it appears that no more than half the spurious wave magnitude is mitigated [38]. To enhance the mitigation of spurious waves, the diagonalisation of the Lagrange multipliers, the relaxation of the Lagrange multipliers coupling condition, or the increase of the overlapping subdomain dimensions were proposed [17,46]. Even damping conditions were also introduced in the overlapping sub-domain [47].

Finally, the approaches proposed hardly succeeded in totally canceling the spurious waves, at least without sacrificing the shock energy conservation or the computational efficiency.

Note that the treatment of spurious waves is voluntarily not adressed in this paper, and a dedicated innovative mathematical spurious wave mitigation method will be proposed in a forthcoming paper.

7.2 | DE subdomain filling and boundaries

The choice of the "Cooker" program, included in the GranOO Workbench [30], was a natural choice to avoid the development of such tool, which involves contact management between discrete elements and domains boundaries. Although developing our own tool dedicated to this study would have enabled the generation of discrete domains with elements center lying on the boudaries, half of the discrete elements would have overlapped with the FE domains, thus leading to additional mass in the model. Another treatment would thus be necessary to weight this mass across the overlapping region, such as using unity partition functions, in a similar way as in the Arlequin method described by Ben Dhia et al. [45]. It would nevertheless be interesting to test this solution to estimate the pros and cons.

8 | CONCLUSION AND PROSPECTS

The paper presents a dynamic remeshing strategy between the FEM and the DEM. This method is based on two approaches aimed at ensuring the spatial and temporal continuity of physical quantities in the problem. Spatial continuity is guaranteed through coupling, which ensures velocity compatibility at interfaces using the Lagrange multipliers method. Temporal continuity is ensured through a field transfer method, where during the replacement of subdomains, the displacements at the FE nodes are interpolated using FE shape functions to the DE nodes. These displacements are then used to determine other fields in the DE. To automate the coupling method and subdomain substitution management, a substitution strategy has been developed.

Numerical examples using the FEM-DEM dynamic remeshing are presented. The first example deals with a simple tensile specimen cracking problem. This case demonstrates realistic crack propagation results and good consistency between domain substitutions and crack path propagation. Additionally, a computation time comparison is made between FEM-DEM remeshing

and fully DEM computations, highlighting the efficiency of the developed method. The second test case involves comparing crack patterns with the Kalthoff experiment, showing that the numerical results closely match those obtained in experiments conducted by Kalthoff.

The dynamic remeshing strategy could be adapted to overlapping couplings if required (coupling enhancement), if/when computation times are affordable, and other future work will deal with the study of the mathematical treatments of waves reflexion. The application of this method cannot be limited to brittle materials. The next step is to apply it to problems involving various non-linearities.

ACKNOWLEDGMENTS

The present research work has been supported by our industrial partner MG-VALDUNES, the Hauts-de-France Region, CNRS, CARNOT ARTS Institute, and LAMIH UMR CNRS 8201 Laboratory. The authors gratefully acknowledge the support of these institutions.

REFERENCES

1. KALTHOFF JF. Shadow Optical Analysis of Dynamic Shear Fracture. *Shadow optical analysis of dynamic shear fracture.* 1988;27(10):835–840.
2. Bui HD, Maigre H, Rittel D. A New Approach to the Experimental Determination of the Dynamic Stress Intensity Factor. *International Journal of Solids and Structures.* 1992;29(23):2881–2895. doi: 10.1016/0020-7683(92)90146-K
3. John R, Shah SP. Mixed-Mode Fracture of Concrete Subjected to Impact Loading. *Journal of Structural Engineering.* 1990;116(3):585–602. doi: 10.1061/(ASCE)0733-9445(1990)116:3(585)
4. Rosakis A. Dynamically Propagating Shear Bands in Impact-Loaded Prenotched Plates—I. Experimental Investigations of Temperature Signatures and Propagation Speed. *Journal of the Mechanics and Physics of Solids.* 1996.
5. Papanastasiou P, Sarris E. 6 - Cohesive Zone Models. In: Shojaei AK, Shao J., eds. *Porous Rock Fracture Mechanics*, , Woodhead Publishing, 2017:119–144
6. Yazid A, Abdelkader N, Abdelmadjid H. A State-of-the-Art Review of the X-FEM for Computational Fracture Mechanics. *Applied Mathematical Modelling.* 2009;33(12):4269–4282. doi: 10.1016/j.apm.2009.02.010
7. Wu JY, Nguyen VP, Nguyen CT, Sutula D, Sinaie S, Bordas SPA. Chapter One - Phase-field Modeling of Fracture. In: Bordas SPA, Balint DS., eds. *Advances in Applied Mechanics*, , . 53. Elsevier, 2020:1–183
8. Hoover C, Bazant Z. Cohesive Crack, Size Effect, Crack Band and Work-of-Fracture Models Compared to Comprehensive Concrete Fracture Tests. *International Journal of Fracture.* 2014;187. doi: 10.1007/s10704-013-9926-0
9. Rabczuk T. Computational Methods for Fracture in Brittle and Quasi-Brittle Solids: State-of-the-Art Review and Future Perspectives. *ISRN Applied Mathematics.* 2013;2013:1–38. doi: 10.1155/2013/849231
10. Kuhn C, Schlüter A, Müller R. On Degradation Functions in Phase Field Fracture Models. *Computational Materials Science.* 2015;108:374–384. doi: 10.1016/j.commatsci.2015.05.034
11. Cundall PA, Strack ODL. A Discrete Numerical Model for Granular Assemblies. *Géotechnique.* 1979;29(1):47–65. doi: 10.1680/geot.1979.29.1.47
12. André D, Iordanoff I, Charles Jl, Néauport J. Discrete Element Method to Simulate Continuous Material by Using the Cohesive Beam Model. *Computer Methods in Applied Mechanics and Engineering.* 2012;213–216:113–125. doi: 10.1016/j.cma.2011.12.002
13. Ibrahimbegovic A, Delaplace A. Microscale and Mesoscale Discrete Models for Dynamic Fracture of Structures Built of Brittle Material. *Computers & Structures.* 2003;81:1255–1265. doi: 10.1016/S0045-7949(03)00040-3
14. Prado E, Mier J. Effect of Particle Structure on Mode I Fracture Process in Concrete. *Engineering Fracture Mechanics - ENG FRACTURE MECH.* 2003;70:1793–1807. doi: 10.1016/S0013-7944(03)00125-5
15. Schlangen E. M&S Highlight: Schlangen and van Mier (1992), Simple Lattice Model for Numerical Simulation of Fracture of Concrete Materials and Structures. *Materials and Structures.* 2022;55(3):95. doi: 10.1617/s11527-022-01932-w
16. André D, Girardot J, Hubert C. A Novel DEM Approach for Modeling Brittle Elastic Media Based on Distinct Lattice Spring Model. *Computer Methods in Applied Mechanics and Engineering.* 2019;350:100–122. doi: 10.1016/j.cma.2019.03.013
17. Xiao S, Belytschko T. A Bridging Domain Method for Coupling Continua with Molecular Dynamics. *Computer Methods in Applied Mechanics and Engineering.* 2004;193(17-20):1645–1669. doi: 10.1016/j.cma.2003.12.053
18. Zhang S, Khare R, Lu Q, Belytschko T. A Bridging Domain and Strain Computation Method for Coupled Atomistic-Continuum Modelling of Solids. 2006:21.
19. Tu F, Ling D, Bu L, Yang Q. Generalized Bridging Domain Method for Coupling Finite Elements with Discrete Elements. *Computer Methods in Applied Mechanics and Engineering.* 2014;276:509–533. doi: 10.1016/j.cma.2014.03.023

20. Tu F, Ling D, Hu C, Zhang R. DEM-FEM Analysis of Soil Failure Process via the Separate Edge Coupling Method: DEM-FEM Analysis of Soil Failure via the Separate Edge Coupling Method. *International Journal for Numerical and Analytical Methods in Geomechanics.* 2017;41(9):1157–1181. doi: 10.1002/nag.2666

21. Chen H, Zang M, Zhang Y. A Ghost Particle-Based Coupling Approach for the Combined Finite-Discrete Element Method. *Finite Elements in Analysis and Design.* 2016;114:68–77. doi: 10.1016/j.finel.2016.02.005

22. Elmekati A, Shamy UE. A Practical Co-Simulation Approach for Multiscale Analysis of Geotechnical Systems. *Computers and Geotechnics.* 2010;37(4):494–503. doi: 10.1016/j.compgeo.2010.02.002

23. Malvar LJ, Warren GE. Mixed Mode Crack Propagation in Concrete. Technical Report N-1807, NAVAL CIVIL ENGINEERING LAB PORT HUENEME CALIFORNIA; 1990.

24. Xu W, Zang M. Four-Point Combined DE/FE Algorithm for Brittle Fracture Analysis of Laminated Glass. *International Journal of Solids and Structures.* 2014;51(10):1890–1900. doi: 10.1016/j.ijsolstr.2014.01.026

25. Frangin E, Marin P, Daudeville L. On the use of combined finite/discrete element method for impacted concrete structures. *Journal de Physique IV (Proceedings).* 2006;134:461–466. doi: 10.1051/jp4:2006134071

26. Rousseau J, Frangin E, Marin P, Daudeville L. Multidomain finite and discrete elements method for impact analysis of a concrete structure. *Engineering Structures.* 2009;31(11):2735–2743. doi: 10.1016/j.engstruct.2009.07.001

27. Tu F, Ling D, Bu L, Yang Q. Generalized Bridging Domain Method for Coupling Finite Elements with Discrete Elements. *Computer Methods in Applied Mechanics and Engineering.* 2014;276:509–533. doi: 10.1016/j.cma.2014.03.023

28. Nikishkov GP. Introduction to the Finite Element Method. *University of Aizu.* 2004:1-70.

29. André D, Iordanoff I, Charles Jl, Néauport J. Discrete Element Method to Simulate Continuous Material by Using the Cohesive Beam Model. *Computer Methods in Applied Mechanics and Engineering.* 2012;213–216:113–125. doi: 10.1016/j.cma.2011.12.002

30. Jebahi M, André D, Terreros I, Iordanoff I. *Discrete Element Method to Model 3D Continuous Materials: Jebahi/Discrete Element Method to Model 3D Continuous Materials*. Hoboken, NJ, USA: John Wiley & Sons, Inc., 2015

31. Casadei F, Leconte N. Coupling Finite Elements and Finite Volumes by Lagrange Multipliers for Explicit Dynamic Fluid–Structure Interaction. *International Journal for Numerical Methods in Engineering.* 2011;86:1–17. doi: 10.1002/nme.3042

32. Chen Z, Wang W, Lévy B, Liu L, Sun F. Revisiting optimal Delaunay triangulation for 3D graded mesh generation. *SIAM Journal on Scientific Computing.* 2014;36(3):A930–A954.

33. Frey PJ, Borouchaki H, George PL. 3D Delaunay mesh generation coupled with an advancing-front approach. *Computer methods in applied mechanics and engineering.* 1998;157(1-2):115–131.

34. Xu Y, Liu K, Ni J, Li Q. 3D Reconstruction Method Based on Second-Order Semiglobal Stereo Matching and Fast Point Positioning Delaunay Triangulation. *PLOS ONE.* 2022;17(1):e0260466. doi: 10.1371/journal.pone.0260466

35. The MathWorks Inc. . MATLAB version: 23.2 (R2023b). 2023.

36. Kalthoff JF. Modes of Dynamic Shear Failure in Solids. *International Journal of Fracture.* 2000;101(1):1–31. doi: 10.1023/A:1007647800529

37. Meng Q, Wang Z. Numerical Simulation of Loading Edge Cracks by Edge Impact Using the Extended Finite Element Method. *Acta Mechanica Solida Sinica.* 2015;28(2):156–167. doi: 10.1016/S0894-9166(15)30004-5

38. Tu F, Ling D, Bu L, Yang Q. Generalized bridging domain method for coupling finite elements with discrete elements. *Computer Methods in Applied Mechanics and Engineering.* 2014;276:509–533. doi: 10.1016/j.cma.2014.03.023

39. Chamoin L, Prudhomme S, Ben Dhia H, Oden T. Ghost forces and spurious effects in atomic-to-continuum coupling methods by the Arlequin approach. *International Journal for Numerical Methods in Engineering.* 2010;83(8-9):1081–1113. doi: 10.1002/nme.2879

40. Wang X, Kulkarni SS, Tabarraei A. Concurrent coupling of peridynamics and classical elasticity for elastodynamic problems. *Computer Methods in Applied Mechanics and Engineering.* 2019;344:251–275. doi: 10.1016/j.cma.2018.09.019

41. Jebahi M, Charles Jl, Dau F, Illoul L, Iordanoff I. 3D coupling approach between discrete and continuum models for dynamic simulations (DEM–CNEM). *Computer Methods in Applied Mechanics and Engineering.* 2013;255:196–209. doi: 10.1016/j.cma.2012.11.021

42. Barros G, Pereira A, Rojek J, Thoeni K. DEM-BEM coupling in time domain for one-dimensional wave propagation. *Engineering Analysis with Boundary Elements.* 2022;135:26–37. doi: 10.1016/j.enganabound.2021.10.017

43. Fung TC. Numerical dissipation in time-step integration algorithms for structural dynamic analysis. *Progress in Structural Engineering and Materials.* 2003;5(3):167–180. doi: 10.1002/pse.149

44. Ramisetti S, Anciaux G, Molinari J. Spatial filters for bridging molecular dynamics with finite elements at finite temperatures. *Computer Methods in Applied Mechanics and Engineering.* 2013;253:28–38. doi: 10.1016/j.cma.2012.09.008

45. Dhia HB, Rateau G. The Arlequin method as a flexible engineering design tool. *International Journal for Numerical Methods in Engineering.* 2005;62(11):1442–1462. doi: 10.1002/nme.1229

46. Frangin E, Marin P, Daudeville L. Approche couplée éléments discrets/finis pour la simulation d'un impact sur ouvrage. *European Journal of Computational Mechanics.* 2007;16(8):989–1009. doi: 10.3166/remn.16.989-1009

47. Sadeghirad A, Tabarraei A. A damping boundary condition for coupled atomistic–continuum simulations. *Computational Mechanics.* 2013;52(3):535–551. doi: 10.1007/s00466-012-0830-7